

Neural Poisson: Indicator Functions for Neural Fields

Angela Dai

Matthias Nießner

Technical University of Munich

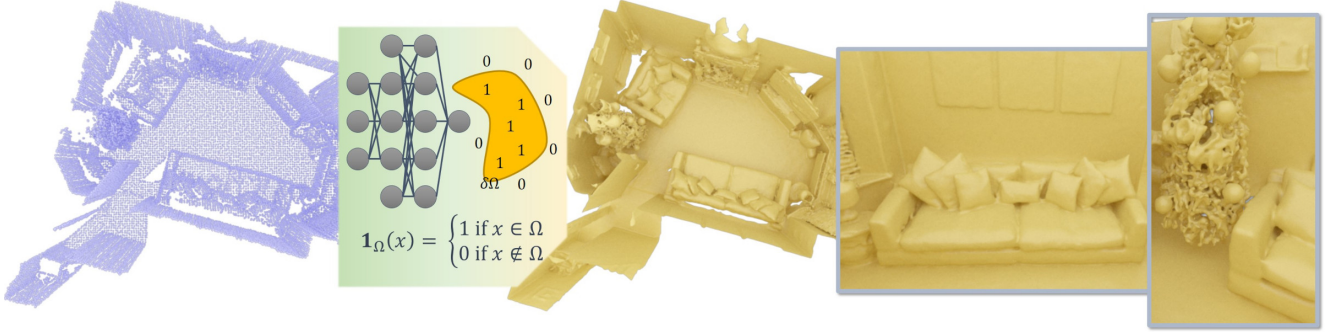


Figure 1. We propose an indicator-based formulation for 3D reconstruction with neural fields. By using neural fields to approximate an indicator function, we can easily incorporate inherent empty space observations from real scan scenarios to produce high-fidelity, accurate surface reconstructions.

Abstract

Implicit neural field generating signed distance field representations (SDFs) of 3D shapes have shown remarkable progress in 3D shape reconstruction and generation. We introduce a new paradigm for neural field representations of 3D scenes; rather than characterizing surfaces as SDFs, we propose a Poisson-inspired characterization for surfaces as indicator functions optimized by neural fields. Crucially, for reconstruction of real scan data, the indicator function representation enables simple and effective constraints based on common range sensing inputs, which indicate empty space based on line of sight. Such empty space information is intrinsic to the scanning process, and incorporating this knowledge enables more accurate surface reconstruction. We show that our approach demonstrates state-of-the-art reconstruction performance on both synthetic and real scanned 3D scene data, with 9.5% improvement in Chamfer distance over state of the art.

1. Introduction

Surface reconstruction has been a fundamental problem in computer vision and graphics, with wide applications to robotics, mixed reality, and content creation. A continuous surface reconstruction enables effective physical reasoning for robot navigation and interaction, with a dense geometric

representation enabling 3D-based semantic inference. Surface geometry representations also fit directly into content creation pipelines, enabling capture of 3D assets from real-world environments. In particular, the ease of availability in acquiring sparse depth measurements of real environments is widespread, e.g., from multi-view images using structure-from-motion pipelines such as COLMAP [25, 26], or range-sensing devices such as the iPhone or Microsoft Kinect. This has driven the need for high-fidelity surface reconstruction from sparse point measurements.

Recently, advances in neural fields have shown remarkable progress in representing 3D shape surfaces [11, 16, 24, 27], by optimizing for functions f such that

$$\{\mathbf{x} \in \mathbb{R}^3 | f(\mathbf{x}, \theta) = 0\},$$

where $f : \mathbb{R}^3 \times \mathbb{R}^n \rightarrow \mathbb{R}$ is characterized by a multilayer perceptron (MLP). In particular, state-of-the-art neural field representations for 3D shape geometry has focused on optimizing for f such that it approximates a signed distance field (SDF) representation of a shape, with its surface at isolevel 0 [11, 24, 27, 33]. High-fidelity reconstructions can be achieved from point observations in which complete object geometry has been observed; however, in real-world scanning scenarios, particularly for large scenes, only partial scans can be acquired, due to complex inter-scene occlusions and physical sensor limitations.

In such real-world scanning scenarios, crucial informa-

tion from the camera pose trajectory – that is, regions of space that are known to be empty as they were observed in front of a surface relative to the camera – has been neglected in these reconstruction formulations. We thus propose a new paradigm for 3D reconstruction with neural field representations, inspired by Poisson-based surface reconstruction techniques [13, 14]. To this end, we characterize surfaces optimized by neural fields as indicator functions, i.e., 0 outside and 1 inside the surface. This is key to our indicator formulation for neural fields with empty space constraints, as values can be constrained to be 0; in contrast, with a distance field representation, empty space can be arbitrary values greater than zero.

In particular, optimization for the indicator function can be characterized by solving for the indicator function whose gradient inverts the normals of the point observations [13]. The neural field formulation enables an efficient optimization of this variational problem, with an elegant way to include additional constraints for empty space regions. In a series of experiments, we demonstrate that our indicator-based formulation for neural field representations for surface reconstruction produces more accurate and detailed reconstructions, improving 9.5% in Chamfer distance over state of the art.

In summary, our contributions are:

- We propose a new, Poisson-inspired indicator formulation for neural fields for high-fidelity surface reconstruction from point data.
- Our indicator formulation enables an elegant incorporation of intrinsic empty space information obtained from real-world scanning processes, for more accurate reconstruction.

2. Related Work

Implicit Neural Field Representations In recent years, neural field representations have been shown to have powerful capability in modeling 3D shape surfaces. Such neural networks implicitly model shape surfaces as level sets of a scalar-output multilayer perceptron that takes as input a coordinate in 3D space [5, 11, 16, 24, 27, 32, 33]. In particular, approximating a signed distance function (SDF) with an MLP has become a popular and effective approach for modeling 3D shapes. DeepSDF [24] approximated SDF representations of 3D shapes through auto-decoder training of an MLP, supervised by explicit computation of the SDF field of complete shape data. Gropp et al. [11] proposed to instead learn SDF approximations by applying an Eikonal loss on the gradient of the MLP, enabling optimization for shape reconstruction based only on observed points. The sine-based MLP approach proposed by Siren [27] further demonstrated the efficacy of sinusoid activations for SDF shape reconstruction leveraging an Eikonal loss. Such MLP-based re-

construction of shape SDFs have also shown to effectively model deformable 3D shapes [22, 23].

Such 3D shape modeling approaches, however, do not consider the extra information given by real-world scanning processes; given a sensor measuring surface points, we can infer that the line of space between the sensor and a surface measurement must be empty of geometry. We thus instead propose to approximate an indicator function rather than an SDF, which enables a simple integration of free space information acquired in real-world scans.

In addition to SDF-based neural field representations for 3D shapes, Occupancy Networks (OccNet) [16] also proposed to approximate an occupancy function with an MLP, supervised with pre-computed point samples in the bounding volume of a complete shape. The sampling-based approximation in its supervision tends to more easily lead to oversmoothed reconstruction results, in comparison to state-of-the-art SDF-based reconstruction. Similar to the SDF-based approaches for neural fields, OccNet does not consider any empty space information in its shape reconstruction. Our indicator-based formulation is instead inspired by the observation from Poisson Surface Reconstruction [13], that oriented point samples can be viewed as samples of the gradient of the indicator function representing the surface.

RGB-D Surface Reconstruction Reconstructing 3D surfaces from discrete range sensing measurements has had a well-studied history in computer graphics and computer vision. Early work fit implicit functions to the point observations with radial basis functions [4, 17, 29] or piecewise polynomial functions [18, 21]. Various methods have also been developed to fit implicit indicator or signed distance field functions by formulating Laplacian systems on tetrahedral [1] and octree representations [3].

Poisson surface reconstruction [13] was a seminal approach to surface reconstruction, which proposed to fit an implicit indicator function to an oriented point set, observing that the gradient of the indicator function must match the inward surface normals at surface points. The optimization is formulated on an octree grid, with the variational problem of approximating the vector field defined by the points transformed into a Poisson problem. Screened poisson surface reconstruction [14] then extended the approach to incorporate constraints directly from the observed points. Our approach is inspired these Poisson surface reconstruction approaches; however, rather than requiring a complex multigrid solver on an octree grid, we leverage the representation power of neural fields to formulate a simple reconstruction optimization that enables a clear incorporation of empty regions given during real-world scanning processes.

Volumetric grid-based reconstruction techniques have also been developed for 3D reconstruction, often incorpo-

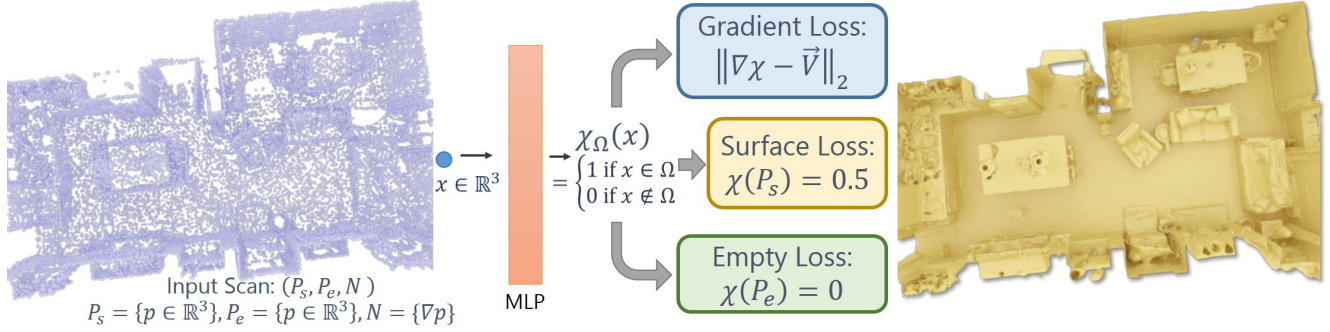


Figure 2. From an input scan of surface observations P_s taken from sensor locations S , we optimize for surface reconstruction with neural field χ approximating an indicator function. From P_s , we can estimate the per-point orientations N and sample empty space regions P_e ; \vec{V} is then estimated as the vector field defined by P_s, N . We formulate surface reconstruction by using an MLP χ to approximate an indicator function. Oriented point observations constrain the surface and gradient of χ , while empty space observations should be 0-valued. This produces an implicit, indicator-based surface reconstruction to accurately reflect input scan observations.

rating empty space knowledge into aggregation of depth map observations into an SDF model of a scanned scene. In particular, real-time 3D reconstruction methods leveraging voxel-based representations have leveraged empty space information from sensor observations in order to carve away spurious surfaces in known free regions [7, 12, 19, 20]. Recent volumetric learning based approaches have also employed empty space information for shape and scene completion tasks [6, 8, 9, 28, 31]. We propose to lift this information away from explicit volumetric representations to a neural field representation not tied to any specific grid resolution, thus avoiding explicit surface point resampling or interpolation, and instead leveraging the implicit regularization properties in neural fields.

3. Indicator-based 3D Neural Fields

Given an input scan taken from sensor locations $S = \{s \in \mathbb{R}^3\}$ with measurements in the form of a point cloud $P_s = \{p \in \mathbb{R}^3\}$, with estimated (inward) normals $N = \{\nabla p \in \mathbb{R}^3\}$, our aim is to optimize for the neural network parameters θ of a neural field MLP $\chi(x, \theta) : \mathbb{R}^3 \times \mathbb{R}^n \rightarrow \mathbb{R}$, such that χ approximates an indicator function representation of a surface $\delta\Omega$ which fits to P_s, N .

That is, the neural field χ takes as input a coordinate $x \in \mathbb{R}^3$, and applies MLP parameters θ to produce a scalar-valued output. We then optimize for θ such that $\chi(x, \theta)$ is close to 1 when $x \in \Omega$ and 0 for $x \notin \Omega$. This enables a compact surface representation not tied to any explicit resolution, from which an explicit mesh representation can be easily extracted through Marching Cubes [15].

In particular, our indicator function formulation enables an elegant optimization formulation for surface reconstruction to unify constraints from input scan observations. We observe that point cloud inputs are captured from sensors that are physically located in an environments; the sensor location in addition to its observed point measurements pro-

vides crucial information about empty space in the scene. Empty space observations are visualized in Figure 3. That is, the line segment between the sensor location s and a point observation p must be empty space, in order for an observation to have occurred no closer than p from s . We thus denote P_e to represent points lying in such free space regions. Given the binary nature of the indicator function representation, this enables us to formulate a novel empty space constraint for points in observed free space regions, $p \in P_e$, which should be 0-valued.

In addition to our empty space constraint, we follow the observation from Poisson Surface Reconstruction [13] that the gradient of the indicator function must be equal to the inward surface normal of the input points at the surface. We thus also constrain the gradient of the estimated indicator function χ to fit the vector field defined by P_s .

Finally, we use the input point samples P_s to encourage the isosurface of χ between 0 and 1 to pass through P_s . The full loss formulation is discussed in Section 4.

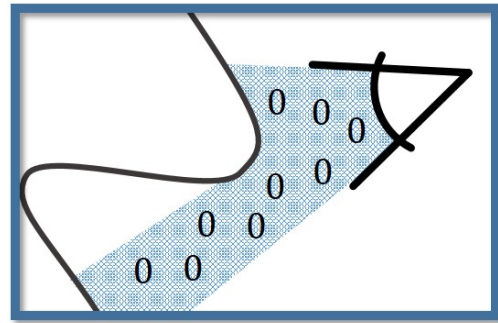


Figure 3. A sensor observing a surface admits observations about empty space. Regions between the sensor and the observed surface must be empty and thus 0-valued, as they precede a surface.

4. Surface Reconstruction Optimization

We aim to optimize for an accurate surface reconstruction as an indicator function represented as a neural field $\chi(x, \theta)$, where χ is an MLP with parameters θ which takes as input $x \in \mathbb{R}^3$ and outputs the approximate indicator function. We constrain χ and its gradient to match the input oriented point observations P_s , in addition to matching empty space given by the input scanning process.

Our loss is thus of the form:

$$L(P_s, P_e, \vec{V}, \theta) = \lambda_g L_g(P_s, \vec{V}, \theta) + \lambda_s L_s(P_s, \theta) + \lambda_e L_e(P_e, \theta), \quad (1)$$

where L_g is a gradient constraint inspired by Poisson Surface Reconstruction [13] to encourage χ to approximate an indicator function (Sec. 4.1), L_s a surface constraint to encourage χ to interpolate input points (Sec. 4.2), and L_e is an empty space constraint (Sec. 4.3) to discourage χ from generating surface in empty regions. $\lambda_g, \lambda_s, \lambda_e$ are scalar weighting factors to balance the loss terms. Note that \vec{V} represents the vector field defined by P_s , which we define in Section 4.4. This enables us to optimize χ to approximate an indicator function.

4.1. Gradient Constraint

The gradient of the estimated indicator function χ should match the vector field defined by the input point observations at the surface, giving

$$L_g(P_s, \vec{V}, \theta) = \|\nabla \chi(p) - \vec{V}(p)\|_2^2, \quad p \in P_s, \quad (2)$$

where \vec{V} is estimated by splatting normals computed from P_s as described in Section 4.4. This inverting of the gradient operator relates to the Poisson Surface Reconstruction formulation [13, 14]; however, our use of stochastic gradient descent on an MLP enables solving for the above constraint without requiring any re-transformations. This results in a very easy-to-implement optimization formulation, in contrast to re-transforming to a Poisson equation, discretization with the Galerkin method on a B-spline basis, and cascaded solve over a multigrid structure [13, 14]. In particular, our neural field formulation obviates the need for optimization over a grid, which is very complex in nature, requiring a multi-grid structure for capturing high resolutions, along with a linear [13] or quadratic [14] interpolation kernel to facilitate gradient approximation. In contrast, gradient computation of the MLP χ can be computed both simply and analytically, through the compute graph of the neural network representation.

4.2. Surface Constraint

Similarly, χ should interpolate the input points P :

$$L_s(P_s, \theta) = \|\chi(p) - 0.5\|_2^2, \quad p \in P_s \quad (3)$$

to encourage its isosurface between 0 and 1 to pass through the points in P . That is, the surface should pass evenly between the 0/1 values at 0.5, so we penalize any deviation of χ from 0.5 at input observed point samples. Similar to the gradient constraint, this loss is very simply applied to the MLP optimization.

4.3. Empty Space Constraint

Finally, points in empty space should be 0-valued:

$$L_e(P_e, \theta) = \|\chi(p)\|_2^2, \quad p \in P_e. \quad (4)$$

This enables incorporation of significant information given simply during the scanning process (as shown in Figure 5) to guide surface reconstruction to avoid observed empty regions. In particular, the indicator-based representation allows for easy characterization of space known to be free of surface geometry, as by definition it should be 0; in contrast, with a signed distance field representation, empty space regions are simply increasing in distance from the surface, which is more difficult to characterize.

4.4. Normal and Gradient Field Estimation

We compute N from P_s by estimating local planes to the surface measurements. When P_s has been acquired as a sequence of depth frames, we leverage the grid structure of the frames to compute normals as a cross product of neighboring camera space positions of the depth values, following RGB-D scanning systems [7, 19, 20]. When P_s is captured as a point set, we estimate N by locally fitting planes to the k -nearest neighbor points for each $p \in P_s$, given by the smallest-eigenvalued eigenvector of a principal component analysis. As normal direction in this scenario is ambiguous, we re-orient all normals to face the sensor location. This provides a sparse set of normals N corresponding to P_s .

For the gradient constraint, since a true indicator function is piecewise constant, its gradient would be unbounded at the surface $\partial\Omega$. We thus instead consider convolving the indicator function with a smoothing filter, and use the gradient of the smoothed indicator function. This is inspired by the Poisson Surface Reconstruction formulation [13], for which we refer to the proof that the gradient of the smoothed indicator function is equal to the vector field obtained by smoothing the normal field.

We then approximate the vector field \vec{V} by applying a filter kernel function F to the input oriented points. This additionally enables us to estimate the values of \vec{V} for regions near the input point observations, providing a degree of surface extrapolation under partial observations.

Then for a location $p \in \mathbb{R}^3$ near the surface points P_s , its normal is estimated by its k -nearest neighbors from P_s . Normals of the k nearest neighbors are clustered by greedy association starting with the closest oriented point, with

each cluster normal represented as a gaussian-weighted average of the cluster element normals. The closest cluster, based on distance to p , then provides its estimated normal as the cluster normal. Empirically, we found this cluster-based approach to provide sharper reconstruction results than a gaussian-weighted average of the k nearest neighbors.

4.5. Empty Space Sampling

To form our empty space constraint, we sample points in regions that are observed to be free based on P_s and the sensor location(s) S . Such sensor information is provided as part of the scanning process, in both commercial scanning products as well as with state-of-the-art RGB-D scanning systems [7, 30]. Thus, for a point $p \in P_s$ observed by a sensor at location s , we sample points q along the ray $s + t(p - s)$. We sample 6 points per ray, of which 2 are sampled close to the observed surface points ($< 0.02\text{m}$), to ensure that empty space is also constrained near the surface points. The sampled points $q \in P_e$ are then subsampled to 1mm resolution, with a maximum of 4 million points.

4.6. Implementation Details

We represent χ as a 5-layer MLP with hidden dimension 256 and sine activation layers [27]. We use empirically determined loss weights $\lambda_g = 1$, $\lambda_s = 100$, and $\lambda_e = 100$ for synthetic data and $\lambda_e = 50$ for real scan data (due to noise in real scan data). For optimization, we use an Adam optimizer with learning rate 0.0001, batch size of 100,000 points each from surface and empty samples, and optimize on a single NVIDIA GeForce GTX 1080 for 40 epochs.

We normalize all input point observations to $[-1, 1]$, and zero-center all output predictions (i.e., instead of 0/1, we estimate a -0.5/0.5 indicator function, with loss constraints shifted accordingly), to better fit the outputs of a sine-based MLP. Additionally, we use $k = 20$ for gradient field estimation, and consider points near surface observations to be < 0.05 from a point in P_s after normalization into $[-1, 1]$.

Meshes are extracted from the optimized χ by applying Marching Cubes [15] at 640^3 resolution samples of χ .

5. Experiments

We demonstrate our approach on both synthetic and real scan data from 3D-FRONT [10] and ARKitScenes [2], respectively. In the synthetic scenario, we use a virtual camera to scan depth sequence observations as input points, and evaluate against the ground truth meshes. We use 100,000 points as input for scans of 3D-FRONT scenes, with point normals estimated from the respective virtually scanned depth maps as in Sec. 4.4. We evaluate 67 randomly sampled scenes from the 3D-FRONT dataset. For real scan data, there are no ground truth meshes available, so we evaluate qualitatively. For ARKitScenes scans, we use the Faro laser

Method	CD (\downarrow)	IoU (\uparrow)	ℓ_2 (\downarrow)
SSD [3]	0.0189	0.504	2.610
SPSR [13, 14]	0.0194	0.505	2.573
SPSR [13, 14] (+trim)	0.0178	0.541	2.293
Siren [27]	0.0183	0.524	2.373
Ours	0.0161	0.545	2.073

Table 1. Evaluation of reconstruction from partial scans of 3D-FRONT [10] scenes. Our indicator-based neural field improves across all metrics in comparison with state-of-the-art traditional and neural network-based reconstruction methods.

measurements sampled at 5mm resolution, with point normals estimated by PCA and re-oriented based on the scanner location(s), as in Sec. 4.4.

Evaluation metrics In order to quantitatively evaluate reconstruction quality when ground truth meshes are available, we consider three measures: chamfer distance (CD), intersection over union (IoU), and ℓ_2 distance. For chamfer distance, 262,144 points are uniformly sampled from reconstructed and ground truth mesh surfaces, with all meshes normalized into the $[-1, 1]$ range. IoU and ℓ_2 distance are computed over voxelization of the predicted and ground truth meshes at 128^3 , with IoU measured on the occupancy voxelization and ℓ_2 as the ℓ_2 distance of the distance field voxelizations (in voxel units), respectively.

Comparison with state of the art We compare with state-of-the-art classical and neural implicit surface reconstruction techniques: screened Poisson surface reconstruction (SPSR) [13, 14] optimizes for an indicator function by directly solving a Poisson equation formulation on an octree representation with the tailored adaptive multigrid solver proposed by the authors; SSD [3] solves a similar variational formulation with an SDF representation; recently, Siren [27] demonstrated state-of-the-art 3D surface reconstruction performance using a neural field representation, approximating an SDF.

Method	CD (\downarrow)	IoU (\uparrow)	ℓ_2 (\downarrow)
SDF	0.0170	0.521	2.173
SDF + High Off-Surface	0.0170	0.518	2.165
Ours (No Empty)	0.0167	0.537	2.132
Ours	0.0161	0.545	2.073

Table 2. Ablation study on reconstruction of partial scans of 3D-FRONT [10] scenes. Our indicator-based formulation improves over optimizing to approximated an SDF, along with optimizing with empty space constraints in a fully complementary fashion.

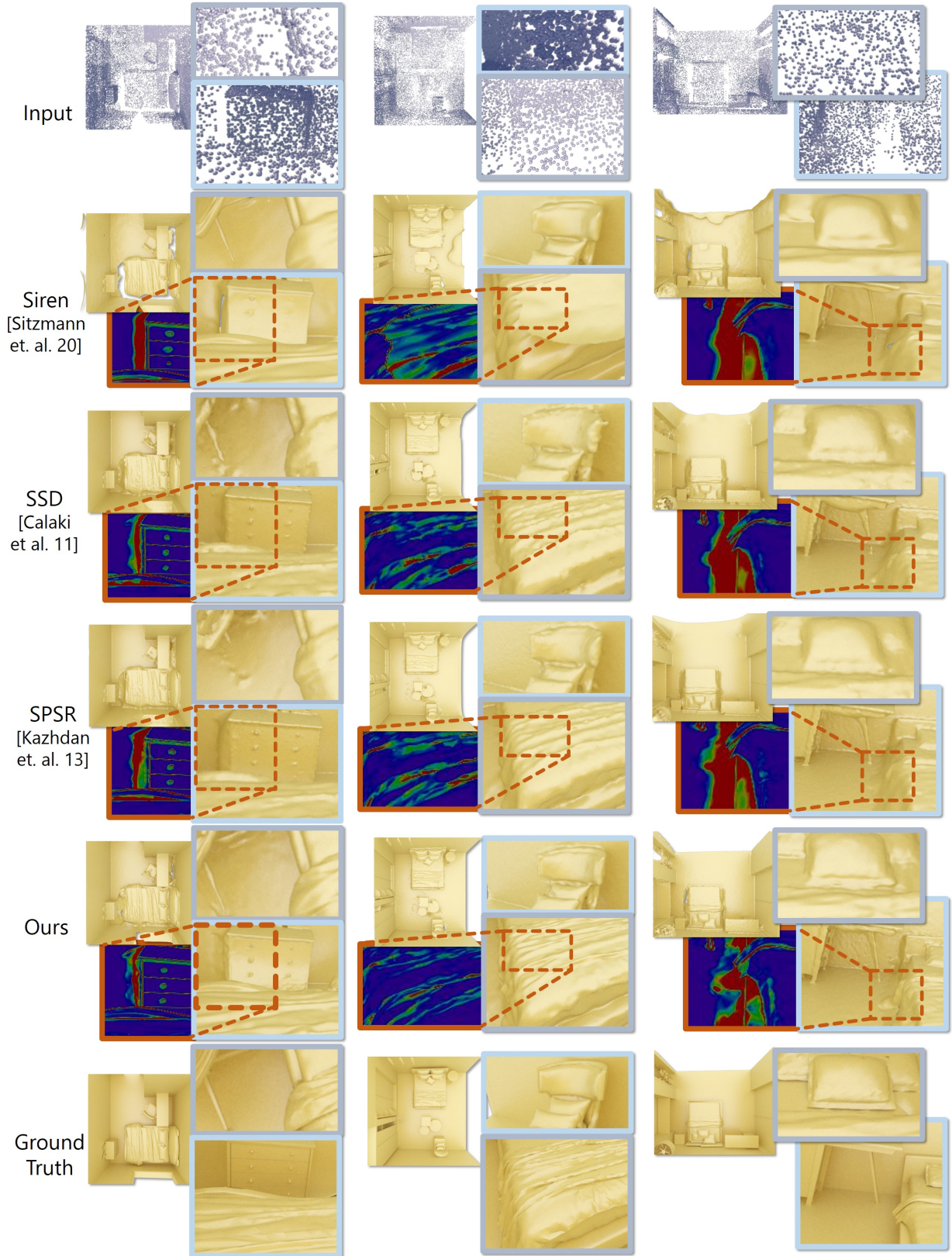


Figure 4. Qualitative evaluation of surface reconstruction on 3D-FRONT [10] scans. Error visualizations (blue 0, red 1) show normal deviation as cosine difference with ground truth in the zoom-in regions. Our indicator-based neural field produces higher-fidelity details along with fewer spurious surfaces.

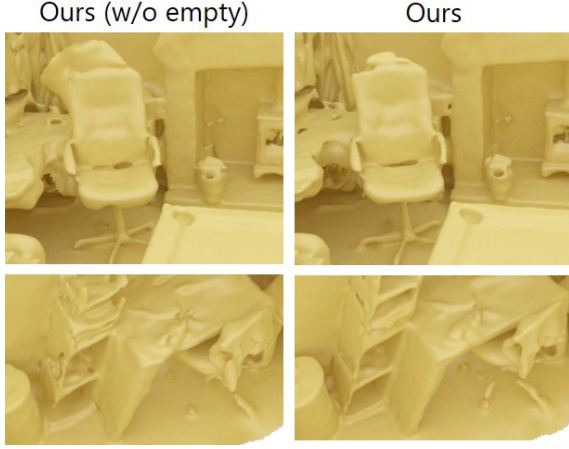


Figure 5. Effect of empty space constraint on real-world ARKitScenes [2] scans. Spurious surface generation is discouraged in observed empty regions, while fidelity is maintained near surface observations due to the near-surface empty space sampling.

Table 1 shows a comparison of our approach to these state-of-the-art methods for surface reconstruction for room-scale scans of 3D-FRONT [10] scenes. Note that since SPSR can generate spurious surfaces in regions of missing data, the official implementation also allows for post-processing trimming of the output reconstruction in regions of low input point density (+trim in Table 1), this can improve the measured reconstruction performance at the cost of removing surface extrapolation. Our indicator-based formulation considering both surface and free space information from the input scans enables more accurate reconstruction than alternatives operating on octree representations or implicit SDF-based neural fields, which do not easily allow for empty space constraints.

We additionally show qualitative reconstruction results on 3D-FRONT scans in Figure 4. Our indicator-inspired formulation with empty space consideration enables reconstruction of finer-scale details (e.g., bed sheet wrinkles) while discouraging spurious surface “ballooning” in known free space (e.g., occluded side of the cabinet, left column).

We further evaluate on 5mm-resolution scans from real-world captured ARKitScenes [2] data in Figure 7. As these scenes were captured in real environments, no ground truth meshes are available, and we show qualitative comparisons with state of the art. Our approach to incorporate free space constraints with an indicator-guided neural field reconstruction enables more precise reconstruction of fine-grained details (e.g., bed frame, bicycles) while mitigating spurious surface generation (e.g., stool, toilet seat).

What is the impact of the indicator formulation? Table 2 evaluates our approach when approximating a signed

distance field output (using an Eikonal loss on the gradients to be 1) rather than an indicator function. Reconstruction quality degrades when estimating an SDF, due to the greater complexity of the representation. Additionally, the SDF representation does not easily admit an empty space constraint, as values off of the surface should be increasing with distance. We can instead emulate an empty space constraint by encouraging non-surface values to be high, using loss constraint $L_{\text{sdf-free}} = \exp(100|\text{SDF}(p)|_1)$ for $p \notin P_s$. This is less precise of a constraint, and does not strictly improve over using SDF only. In contrast, our approach improves across all reconstruction quality measures when incorporating the empty space constraint.

What is the effect of the empty space constraint? Table 2 shows that incorporating knowledge of free space given by the scanning process improves performance across all reconstruction metrics. The effect is visualized in Figure 5: our empty space constraint discourages spurious surface generation in observed empty regions, while maintaining high fidelity near surface observations due to the near-surface empty space sampling.

Effect of number of input points. We additionally analyze the effect of the number of input points samples per scene on 3D-FRONT [10] data in Figure 6. Under varying degrees of sparser input point sampling, our approach nonetheless still consistently outperforms all baselines.

Limitations and Future Work Our approach shows an effective incorporation of intrinsic scanning information for surface reconstruction; however, several limitations remain. For instance, significant noise in the sensor pose estimation could lead to notable conflict between estimated empty space and surface regions. In this context, it would be interesting to jointly solve for camera poses as part of the re-

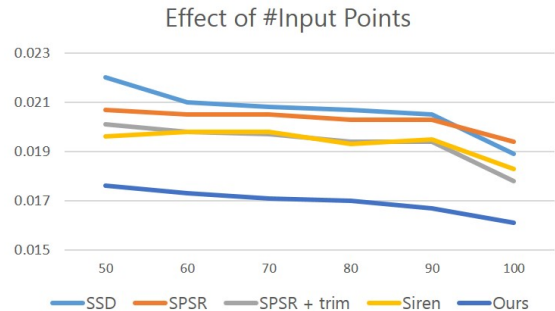


Figure 6. Comparison against state of the art when varying the number of input points ($[50, 60, 70, 80, 90, 100] \times 10^3$). We measure Chamfer distance. Our indicator-based neural field consistently outperforms baselines, even under sparser point sampling.

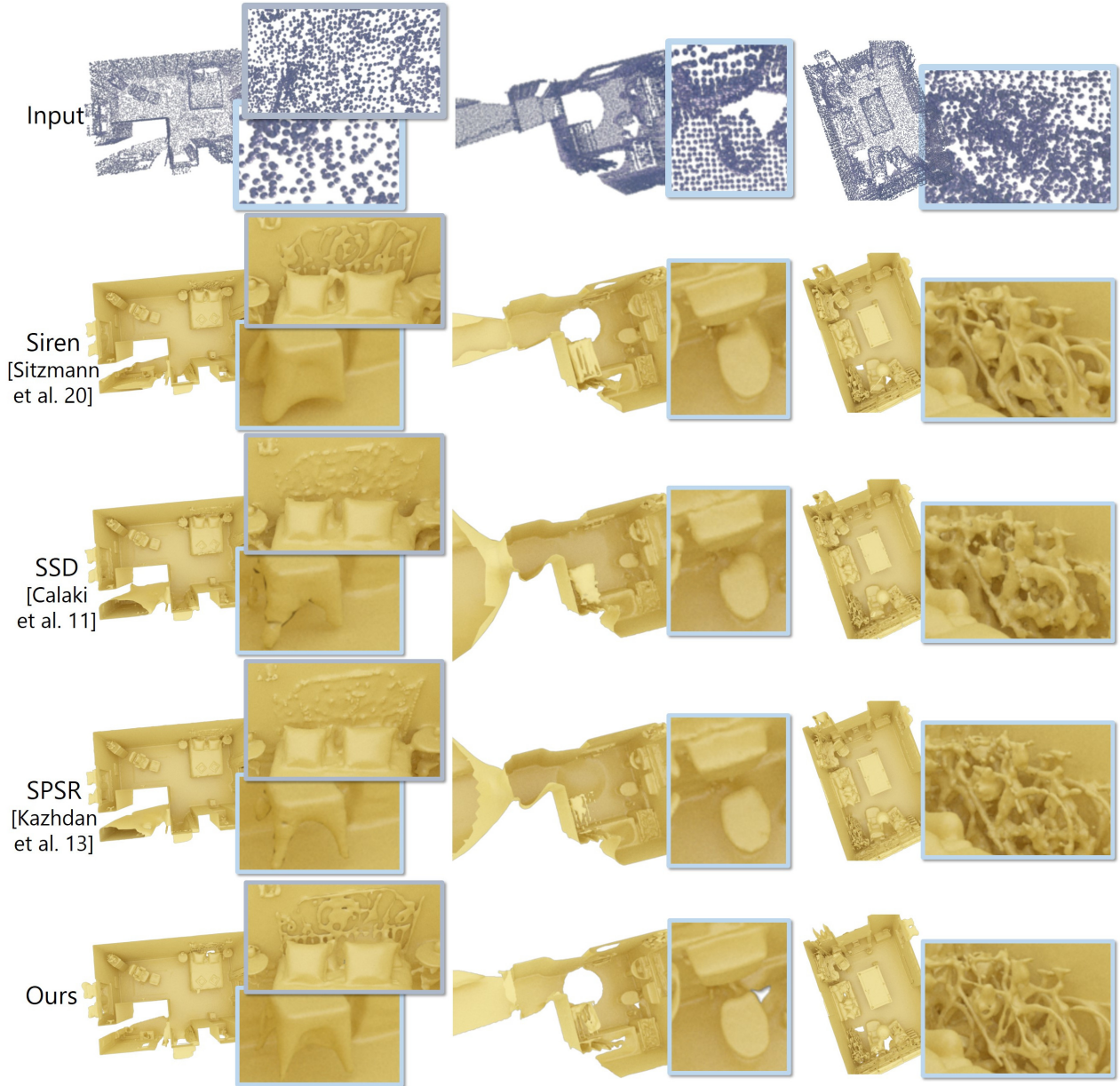


Figure 7. Qualitative evaluation of surface reconstruction on real ARKitScenes [2] scans. Our indicator-based neural field maintains finer-grained details (e.g., bed frame, toilet pipe, bicycles) while avoiding spurious generation in observed empty regions (e.g., stool, toilet seat).

construction process. Additionally, while any surface extrapolation is discouraged to lie in observed free space, it will be pushed towards unobserved regions of space, which remains under-determined with respect to the true surface geometry. Incorporation of a data-driven prior could improve general extrapolation behavior, for instance, learned based on the underlying semantics of the input point cloud.

6. Conclusion

We introduce a new indicator-based paradigm for 3D reconstruction with neural field representations. In contrast to the conventional approximation for reconstruction with signed distance fields, our indicator representation admits a simple and effective surface reconstruction formulation to consider both surface observation constraints as well as empty space constraints, which are not easily represented in state-of-the-art alternatives. This enables more accurate reconstruction in large-scale scanning scenarios. We be-

lieve this perspective on the popular neural field representation for modeling 3D surfaces will provide new avenues in 3D reconstruction; e.g., when combining traditional reconstruction methods with learning-based techniques.

Acknowledgments

This work was supported by the Bavarian State Ministry of Science and the Arts coordinated by the Bavarian Research Institute for Digital Transformation (bidt), the ERC Starting Grant Scan2CAD (804724), the German Research Foundation (DFG) Grant “Making Machine Learning on Static and Dynamic 3D Data Practical”, and the German Research Foundation (DFG) Research Unit “Learning and Simulation in Visual Computing.”

References

- [1] Pierre Alliez, David Cohen-Steiner, Yiying Tong, and Mathieu Desbrun. Voronoi-based variational reconstruction of un-oriented point sets. In *Symposium on Geometry processing*, volume 7, pages 39–48, 2007. [2](#)
- [2] Gilad Baruch, Zhuoyuan Chen, Afshin Dehghan, Tal Dimry, Yuri Feigin, Peter Fu, Thomas Gebauer, Brandon Joffe, Daniel Kurz, Arik Schwartz, and Elad Shulman. ARK-scenes - a diverse real-world dataset for 3d indoor scene understanding using mobile RGB-d data. In *Thirty-fifth Conference on Neural Information Processing Systems Datasets and Benchmarks Track (Round 1)*, 2021. [5](#), [7](#), [8](#), [11](#), [12](#)
- [3] Fatih Calakli and Gabriel Taubin. Ssd: Smooth signed distance surface reconstruction. In *Computer Graphics Forum*, volume 30, pages 1993–2002. Wiley Online Library, 2011. [2](#), [5](#), [11](#)
- [4] Jonathan C Carr, Richard K Beatson, Jon B Cherrie, Tim J Mitchell, W Richard Fright, Bruce C McCallum, and Tim R Evans. Reconstruction and representation of 3d objects with radial basis functions. In *Proceedings of the 28th annual conference on Computer graphics and interactive techniques*, pages 67–76, 2001. [2](#)
- [5] Julian Chibane, Thiemo Alldieck, and Gerard Pons-Moll. Implicit functions in feature space for 3d shape reconstruction and completion. In *Proceedings of the IEEE/CVF Conference on Computer Vision and Pattern Recognition*, pages 6970–6981, 2020. [2](#)
- [6] Angela Dai, Christian Diller, and Matthias Nießner. Sg-nn: Sparse generative neural networks for self-supervised scene completion of rgb-d scans. In *Proc. Computer Vision and Pattern Recognition (CVPR), IEEE*, 2020. [3](#)
- [7] Angela Dai, Matthias Nießner, Michael Zollhöfer, Shahram Izadi, and Christian Theobalt. Bundlefusion: Real-time globally consistent 3d reconstruction using on-the-fly surface reintegration. *ACM Trans. Graph.*, 36(3):24:1–24:18, 2017. [3](#), [4](#), [5](#), [11](#)
- [8] Angela Dai, Charles Ruizhongtai Qi, and Matthias Nießner. Shape completion using 3d-encoder-predictor cnns and shape synthesis. In *2017 IEEE Conference on Computer Vision and Pattern Recognition, CVPR 2017, Honolulu, HI, USA, July 21-26, 2017*, pages 6545–6554, 2017. [3](#)
- [9] Angela Dai, Daniel Ritchie, Martin Bokeloh, Scott Reed, Jürgen Sturm, and Matthias Nießner. Scancomplete: Large-scale scene completion and semantic segmentation for 3d scans. In *2018 IEEE Conference on Computer Vision and Pattern Recognition, CVPR 2018, Salt Lake City, UT, USA, June 18-22, 2018*, pages 4578–4587, 2018. [3](#)
- [10] Huan Fu, Bowen Cai, Lin Gao, Ling-Xiao Zhang, Jiaming Wang, Cao Li, Qixun Zeng, Chengyue Sun, Rongfei Jia, Bin-qiang Zhao, et al. 3d-front: 3d furnished rooms with layouts and semantics. In *Proceedings of the IEEE/CVF International Conference on Computer Vision*, pages 10933–10942, 2021. [5](#), [6](#), [7](#), [11](#)
- [11] Amos Gropp, Lior Yariv, Niv Haim, Matan Atzmon, and Yaron Lipman. Implicit geometric regularization for learning shapes. In *Proceedings of Machine Learning and Systems 2020*, pages 3569–3579. 2020. [1](#), [2](#)
- [12] Shahram Izadi, David Kim, Otmar Hilliges, David Molyneaux, Richard A. Newcombe, Pushmeet Kohli, Jamie Shotton, Steve Hodges, Dustin Freeman, Andrew J. Davison, and Andrew W. Fitzgibbon. Kinectfusion: real-time 3d reconstruction and interaction using a moving depth camera. In *Proceedings of the 24th Annual ACM Symposium on User Interface Software and Technology, Santa Barbara, CA, USA, October 16-19, 2011*, pages 559–568, 2011. [3](#)
- [13] Michael Kazhdan, Matthew Bolitho, and Hugues Hoppe. Poisson surface reconstruction. In *Proceedings of the fourth Eurographics symposium on Geometry processing*, volume 7, 2006. [2](#), [3](#), [4](#), [5](#), [11](#)
- [14] Michael Kazhdan and Hugues Hoppe. Screened poisson surface reconstruction. *ACM Transactions on Graphics (ToG)*, 32(3):1–13, 2013. [2](#), [4](#), [5](#), [11](#)
- [15] William E. Lorensen and Harvey E. Cline. Marching cubes: A high resolution 3d surface construction algorithm. In *Proceedings of the 14th Annual Conference on Computer Graphics and Interactive Techniques, SIGGRAPH 1987, Anaheim, California, USA, July 27-31, 1987*, pages 163–169, 1987. [3](#), [5](#)
- [16] Lars Mescheder, Michael Oechsle, Michael Niemeyer, Sebastian Nowozin, and Andreas Geiger. Occupancy networks: Learning 3d reconstruction in function space. In *Proceedings of the IEEE/CVF conference on computer vision and pattern recognition*, pages 4460–4470, 2019. [1](#), [2](#)
- [17] Shigeru Muraki. Volumetric shape description of range data using “blobby model”. In *Proceedings of the 18th annual conference on Computer graphics and interactive techniques*, pages 227–235, 1991. [2](#)
- [18] Yukie Nagai, Yutaka Ohtake, and Hiromasa Suzuki. Smoothing of partition of unity implicit surfaces for noise robust surface reconstruction. In *Computer Graphics Forum*, volume 28, pages 1339–1348. Wiley Online Library, 2009. [2](#)
- [19] Richard A. Newcombe, Shahram Izadi, Otmar Hilliges, David Molyneaux, David Kim, Andrew J. Davison, Pushmeet Kohli, Jamie Shotton, Steve Hodges, and Andrew W. Fitzgibbon. Kinectfusion: Real-time dense surface mapping and tracking. In *10th IEEE International Symposium on Mixed and Augmented Reality, ISMAR 2011, Basel, Switzerland, October 26-29, 2011*, pages 127–136, 2011. [3](#), [4](#), [11](#)

- [20] M. Nießner, M. Zollhöfer, S. Izadi, and M. Stamminger. Real-time 3d reconstruction at scale using voxel hashing. *ACM Transactions on Graphics (TOG)*, 2013. 3, 4, 11
- [21] Yutaka Ohtake, Alexander Belyaev, and Marc Alexa. Sparse low-degree implicit surfaces with applications to high quality rendering, feature extraction, and smoothing. In *Proc. Symp. Geometry Processing*, pages 149–158, 2005. 2
- [22] Pablo Palafox, Aljaž Božič, Justus Thies, Matthias Nießner, and Angela Dai. Npms: Neural parametric models for 3d deformable shapes. In *Proceedings of the IEEE/CVF International Conference on Computer Vision*, pages 12695–12705, 2021. 2
- [23] Pablo Palafox, Nikolaos Sarafianos, Tony Tung, and Angela Dai. Spams: Structured implicit parametric models. In *Proceedings of the IEEE/CVF Conference on Computer Vision and Pattern Recognition*, pages 12851–12860, 2022. 2
- [24] Jeong Joon Park, Peter Florence, Julian Straub, Richard Newcombe, and Steven Lovegrove. DeepSDF: Learning continuous signed distance functions for shape representation. In *Proceedings of the IEEE/CVF conference on computer vision and pattern recognition*, pages 165–174, 2019. 1, 2
- [25] Johannes Lutz Schönberger and Jan-Michael Frahm. Structure-from-motion revisited. In *Conference on Computer Vision and Pattern Recognition (CVPR)*, 2016. 1
- [26] Johannes Lutz Schönberger, Enliang Zheng, Marc Pollefeys, and Jan-Michael Frahm. Pixelwise view selection for unstructured multi-view stereo. In *European Conference on Computer Vision (ECCV)*, 2016. 1
- [27] Vincent Sitzmann, Julien Martel, Alexander Bergman, David Lindell, and Gordon Wetzstein. Implicit neural representations with periodic activation functions. *Advances in Neural Information Processing Systems*, 33:7462–7473, 2020. 1, 2, 5, 11
- [28] Shuran Song, Fisher Yu, Andy Zeng, Angel X Chang, Manolis Savva, and Thomas Funkhouser. Semantic scene completion from a single depth image. In *Proceedings of the IEEE conference on computer vision and pattern recognition*, pages 1746–1754, 2017. 3
- [29] Greg Turk and James F O’Brien. Modelling with implicit surfaces that interpolate. *ACM Transactions on Graphics (TOG)*, 21(4):855–873, 2002. 2
- [30] Thomas Whelan, Stefan Leutenegger, Renato F. Salas-Moreno, Ben Glocker, and Andrew J. Davison. Elasticfusion: Dense SLAM without A pose graph. In *Robotics: Science and Systems XI, Sapienza University of Rome, Rome, Italy, July 13-17, 2015*, 2015. 5
- [31] Zhirong Wu, Shuran Song, Aditya Khosla, Fisher Yu, Linguang Zhang, Xiaoou Tang, and Jianxiong Xiao. 3d shapenets: A deep representation for volumetric shapes. In *IEEE Conference on Computer Vision and Pattern Recognition, CVPR 2015, Boston, MA, USA, June 7-12, 2015*, pages 1912–1920, 2015. 3
- [32] Yiheng Xie, Towaki Takikawa, Shunsuke Saito, Or Litany, Shiqin Yan, Numair Khan, Federico Tombari, James Tompkin, Vincent Sitzmann, and Srinath Sridhar. Neural fields in visual computing and beyond. In *Computer Graphics Forum*, volume 41, pages 641–676. Wiley Online Library, 2022. 2
- [33] Wang Yifan, Shihao Wu, Cengiz Oztireli, and Olga Sorkine-Hornung. Iso-points: Optimizing neural implicit surfaces with hybrid representations. In *Proceedings of the IEEE/CVF Conference on Computer Vision and Pattern Recognition*, pages 374–383, 2021. 1, 2

A. Additional Qualitative Results

Figure 8 shows additional qualitative surface reconstruction results of our method on real-world ARKitScenes [2] scans. Our approach can effectively reconstruct smaller-scale structures such as tree in first row and the chair legs in bottom two rows.

B. Additional Data Details

To generate input data from the synthetic 3D scenes of the 3D-FRONT [10] dataset, we sample virtual cameras in each scene, approximately 1.5 meters from each other, and facing frontwards, tilted upwards 30 degrees, and tilted downwards 30 degrees. Depth maps are then extracted from rendered sensor images as input points. For each depth map, we use the grid structure of the depth image to compute normals; we compute camera space coordinates for each pixel using the camera intrinsic projection, and estimate normals as a cross product of the neighboring camera space positions. This procedure follows state-of-the-art RGB-D scanning systems [7, 19, 20]. Finally, all input points are randomly subsampled to 100,000 points per scene.

C. Additional Baseline Details

All methods were run on the same set of input points P_s and estimated normals \tilde{N} used as input to our method.

Screened Poisson Surface Reconstruction (SPSR) [13, 14] We used the authors’ public implementation for SPSR¹. SPSR was run at a depth of 9 for 3D-FRONT scans, and a depth of 10 for ARKitScenes scans, which we empirically found to perform the best for the respective data. We follow with optional surface trimming from the authors’ repository at a threshold of 6 (+trim in the main evaluation), which removes output geometry in regions of low input point density.

Smooth Signed Distance Surface Reconstruction (SSD) [3] We used the authors’ public implementation for SSD². We run SSD at an octree maximum depth of 10 with weights $\lambda_0 = 10, \lambda_1 = 1, \lambda_2 = 1$ for the surface, gradient, and regularization energy terms, respectively, which we empirically found produce the best results for both datasets.

Siren [27] We used the authors’ public implementation of Siren³. We optimize for 18,000 epochs at a batch size of 100,000 points for a 5-layer MLP with 256 hidden units per

layer. We follow the learning rate and loss weights provided by the authors for the 3D reconstruction task.

¹<https://github.com/mkazhdan/PoissonRecon>

²<http://mesh.brown.edu/ssd/software.html>

³<https://github.com/vsitzmann/siren>

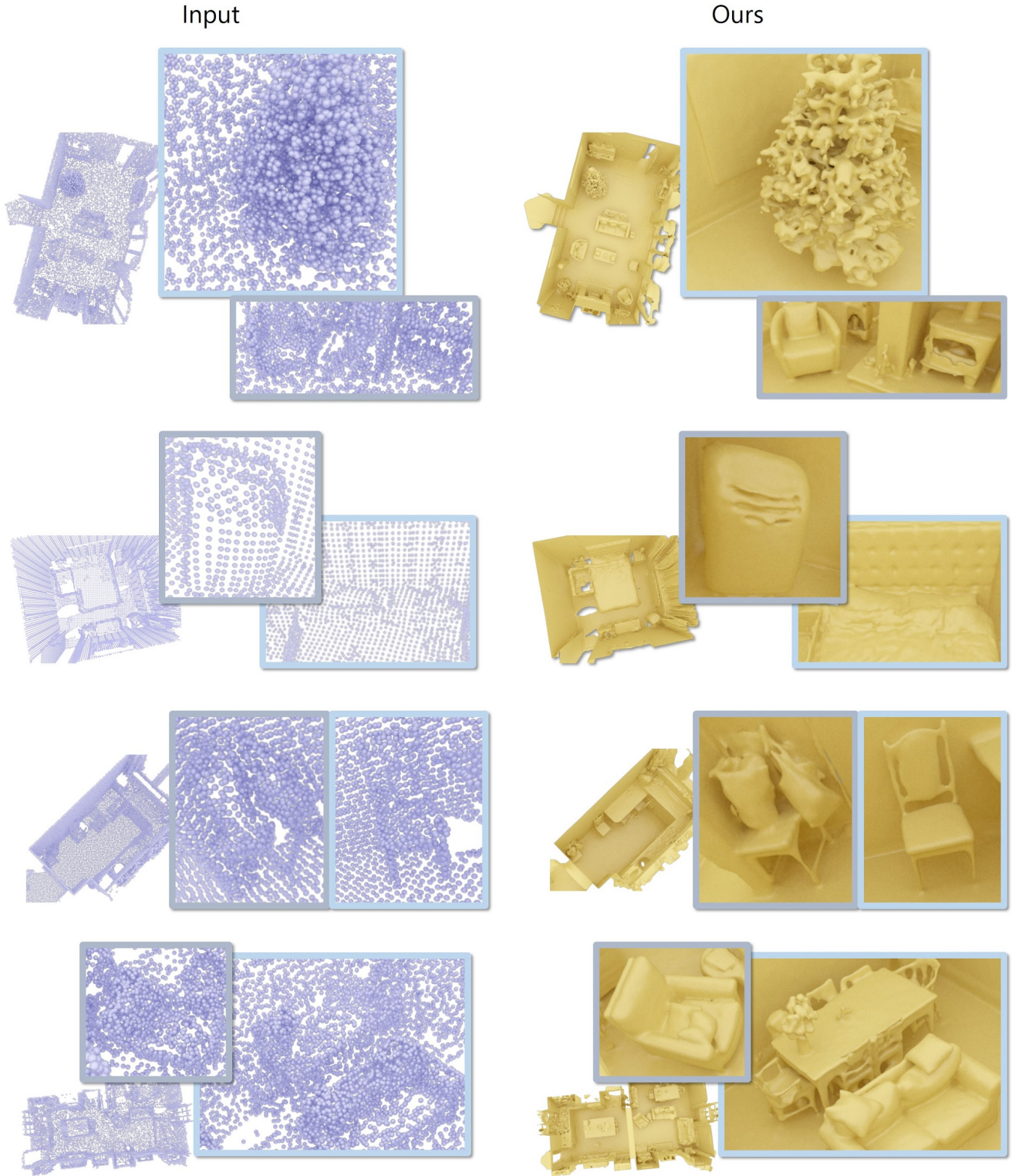


Figure 8. Additional qualitative surface reconstruction results on real scans from ARKitScenes [2]. Our indicator-based neural field achieves high fidelity reconstruction for finer-scale details (e.g., tree, chair legs) and global structures.